RSC Advances

PAPER

View Article Online
View Journal | View Issue

Cite this: *RSC Adv.*, 2020, **10**, 43343

Spin-state dependence of the structural and vibrational properties of solvated iron(II) polypyridyl complexes from AIMD simulations: III. $[Fe(tpen)]Cl_2$ in acetonitrile†

Latévi M. Lawson Daku

In order to achieve an in-depth understanding of the role played by the solvent in the photoinduced low-spin (LS) → high-spin (HS) transition in solvated Fe(II) complexes, an accurate description of the solvated complexes in the two spin states is required. To this end, we are applying state-of-the-art *ab initio* molecular dynamics (AIMD) simulations to the study of the structural and vibrational properties of iron(II) polypyridyl complexes. Two aqueous LS complexes were investigated in this framework, namely, $[Fe(bpy)_3]^{2+}$ (bpy = 2,2′-bipyridine) [Lawson Daku and Hauser, *J. Phys. Chem. Lett.*, 2010, **1**, 1830; Lawson Daku, *Phys. Chem. Chem. Phys.*, 2018, **20**, 6236] and $[Fe(tpy)_2]^{2+}$ (tpy = 2,2′:6′,2″-ter-pyridine) [Lawson Daku, *Phys. Chem. Chem. Phys.*, 2019, **21**, 650]. For aqueous $[Fe(bpy)_3]^{2+}$, combining the results of forefront wide-angle X-ray scattering experiments with those of the AIMD simulations allowed the visualization of the interlaced coordination and solvation spheres of the photoinduced HS state [Khakhulin *et al.*, *Phys. Chem. Chem. Phys.*, 2019, **21**, 9277]. In this paper, we report the extension of our AIMD studies to the spin-crossover complex $[Fe(tpen)]^{2+}$ (tpen = *N*,*N*,*N*′,*N*′-tetrakis(2-pyridylmethyl) ethylenediamine) in acetonitrile (ACN). The determined LS and HS solution structures of the complex are in excellent agreement with the experimental results obtained by high-resolution transient X-ray absorption spectroscopy [Zhang *et al.*, *ACS Omega*, 2019, **4**, 6375]. The first solvation shell of $[Fe(tpen)]^{2+}$ consists of ACN molecules located in the grooves defined by the chelating coordination motif of the tpen ligand. Upon the LS → HS change of states, the solvation number of the complex is found to increase from ≈9.2 to ≈11.9 and an inner solvation shell is formed. This inner solvation shell originates from the occupancy by about one ACN molecule of the internal cavity which results from the arrangement of the 4 pyridine rings of the tpen ligand, and which becomes accessible to the solvent molecules in the HS state only thanks to the structural changes undergone by the complex. The presence of this inner solvation shell for the solvated HS complex probably plays a key role in the spin-state dependent reactivity of $[Fe(tpen)]^{2+}$ in liquid solutions.

Received 8th November 2020
Accepted 19th November 2020

DOI: 10.1039/d0ra09499d

rsc.li/rsc-advances

1 Introduction

The accurate description of transition metal complexes in liquid solutions is a challenging fundamental research problem, which must be tackled in order to achieve an in-depth understanding of the role played by the solvent in the photo-induced low-spin (LS) → high-spin (HS) transition in solvated hexacoordinated Fe(II) complexes. These complexes can indeed exhibit the phenomenon of spin crossover (SCO), that is the entropy-driven thermal depopulation of their ligand-field LS electronic ground state of octahedral $^1A_1(t_{2g}^6)$ parentage in favor of their ligand-field HS metastable state of octahedral $^5T_2(t_{2g}^4e_g^2)$ parentage.[1] Light irradiation can also be used to induce the LS ⇄ HS change of states in both SCO and so-called LS complexes whose HS state lies too high in energy to be thermally populated.[2–4] SCO complexes with a large energy barrier between the two states also show the phenomenon of light-induced excited spin-state trapping (LIESST), wherein the complexes become trapped in the HS state because the HS → LS relaxation following the photoinduced population of the HS state become too slow at low temperatures.[3,4] The ability to use

Département de Chimie Physique, Université de Genève, Quai E. Ansermet 30, CH-1211 Genève 4, Switzerland. E-mail: max.lawson@unige.ch

† Electronic supplementary information (ESI) available: Distribution functions of the angles Π_1 and Π_2. Distribution functions of the Fe–C_iFe≡C_i' ($i = 1, \ldots, 7$) distances. Distribution functions of the Fe–C_ζ ($\zeta = \beta, \gamma, \delta$) distances. Snapshots from the HS trajectory showing ACN molecules in the inner solvation shell of HS $[Fe(tpen)]^{2+}$. Radial distribution functions characterizing the structure of the acetonitrile solvent for $[Fe(tpen)]^{2+}$ in the LS and HS states. Snapshots from the LS trajectory illustrating the first solvation shell of the Cl^- counterions. Time dependence of the Fe–Cl distances for $[Fe(tpen)]^{2+}$ in the LS and HS states. IR spectrum of the ACN solvent. Comparison between the IR spectra of $[Fe(tpen)]Cl_2$ and $[Fe(tpen)]^{2+}$ in ACN. See DOI: 10.1039/d0ra09499d

light irradiation to control the spin state of these complexes makes them ideal candidates for the studies of fundamental photophysical processes in transition metal complexes.[5–7]

The mechanism of the photoinduced LS → HS change of states is thus being thoroughly investigated for SCO and LS Fe(II) polypyridyl complexes in solution using ultrafast vibrational,[8–10] UV-vis,[10–17] and X-ray[18–40] spectroscopies. This way, new insights are being gained into the electronic state dynamics and into the structural dynamics of the $Fe^{II}N_6$ core, which includes the accurate determination of the changes in the Fe–N bond lengths. And, recently, advances in the understanding of the ultrafast photoinduced dynamics in a solvated [2 × 2] iron(II) metallogrid could be achieved by combining the three types of ultrafast spectroscopies.[41] However, these ultrafast spectroscopy studies tend to leave open questions regarding the evolution of the whole molecular edifice, the influence of the solvent on the becoming of the photoexcited complex and the response of the solvation shell. Answering these questions requires an accurate description of the complexes in solution. To this end, we have undertaken a series of studies wherein we apply state-of-the-art *ab initio* molecular dynamics (AIMD) simulations to the study of the spin-state dependence of the structural and vibrational properties of solvated iron(II) polypyridyl complexes. We have studied the prototypical LS $[Fe(bpy)_3]^{2+}$ (bpy = 2,2′-bipyridine) complex in water.[42,43] The results obtained have proved to constitute current reference data for classical MD studies[44,45] and experimental data analysis.[26,33–35] Actually, the combination of the AIMD simulations with forefront X-ray absorption spectroscopy (XAS) and wide-angle X-ray scattering (WAXS) experiments allowed the visualization of the interlaced coordination and solvation spheres of the aqueous $[Fe(bpy)_3]^{2+}$ in the photoinduced HS state.[38] We have also investigated the aqueous LS $[Fe(tpy)_2]^{2+}$ (tpy = 2,2′:6′,2″-ter-pyridine) complex.[46] The comparison of the results similarly obtained for the chemically close LS complexes $[Fe(tpy)_2]^{2+}$ and $[Fe(bpy)_3]^{2+}$ allowed to probe the influence of the coordination motif (tetragonal *versus* trigonal) on their hydration structure. In this paper, we extend our AIMD studies to a SCO complex in acetonitrile (ACN), namely, $[Fe(tpen)]^{2+}$ where tpen denotes the hexadentate *N*,*N*,*N*′,*N*′-tetrakis(2-pyridylmethyl)ethylenediamine ligand.[47] With its distinct molecular architecture and the presence of inequivalent metal–ligand bonds, $[Fe(tpen)]^{2+}$ is a very attractive transition metal system for fundamental photophysical studies; and, in this respect, the photoinduced LS → HS change of states has been investigated for $[Fe(tpen)]^{2+}$ in ACN by high-resolution transient X-ray absorption spectroscopy (TXAS).[37] Interestingly also, the racemization of the solvated complex is proposed to be coupled with the SCO equilibrium.[48–51] Furthermore $[Fe(tpen)]^{2+}$ exhibits in liquid solutions a spin-state dependent reactivity towards superoxide, dioxygen and nitric oxide,[52–54] which remains to be fully understood. In terms of structure–properties relationships, this raises the question as to know which structural modifications entailed by the change of spin states can explain the spin-state dependence of these reactions. Consequently, with the present AIMD study of $[Fe(tpen)]^{2+}$ in ACN, we aim at achieving an accurate description of the $[Fe(tpen)]^{2+}$ solution in the LS and in the HS state, from which a first insight could also be gained into the origin of this spin-state dependent reactivity.

2 Computational details

The studied system consists of one $[Fe(tpen)]^{2+}$ complex, 2 Cl^- counterions and 109 acetonitrile molecules in a cubic box of side 23 Å (Fig. 1).

2.1 Initial configurations

The initial LS configuration was obtained from a preliminary classical MD simulation of 1 ns duration followed by an optimization performed within DFT using the theoretical level described below. The classical MD simulation was run at 300 K with the GROMACS program package[55,56] using the OPLS all-atom (OPLS-AA) force field for describing the Cl^- ions and the ACN solvent molecules,[57–62] and employing for the description of LS $[Fe(tpen)]^{2+}$ kept fixed to its optimized geometry[37] an approximate approximate model generated with the MKTOP program.[63] The initial HS configuration was obtained from a DFT optimization performed in the HS state using a snapshot of the LS production trajectory as starting point.

2.2 BOMD simulations

The settings are similar to those used in our previous BOMD studies.[43,46] The simulations were thus performed with the dispersion-corrected BLYP-D3 functional[64–66] and the hybrid Gaussian and planewave (GPW) method[67] as implemented in the CP2K/QUICKSTEP program.[68] The core electrons of the

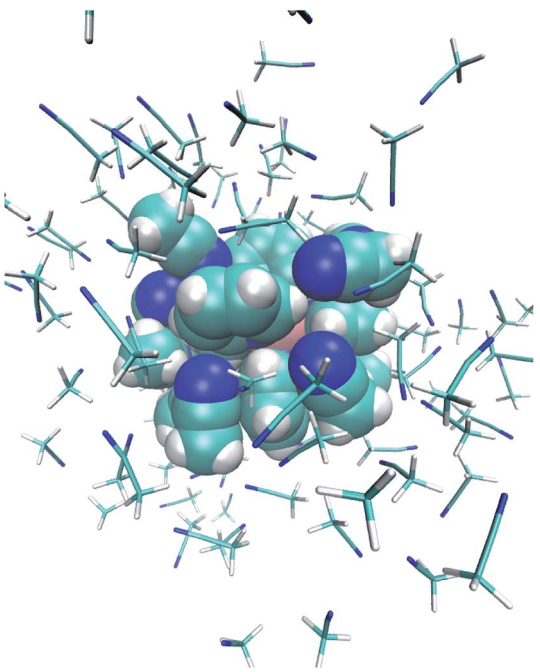

Fig. 1 Snapshot from the HS trajectory (t = 6662.5 fs): $[Fe(tpen)]^{2+}$ and the ACN molecules in its first solvation shell are drawn with a van der Waals representation, and the ACN molecules located beyond the first solvation shell with a licorice representation.

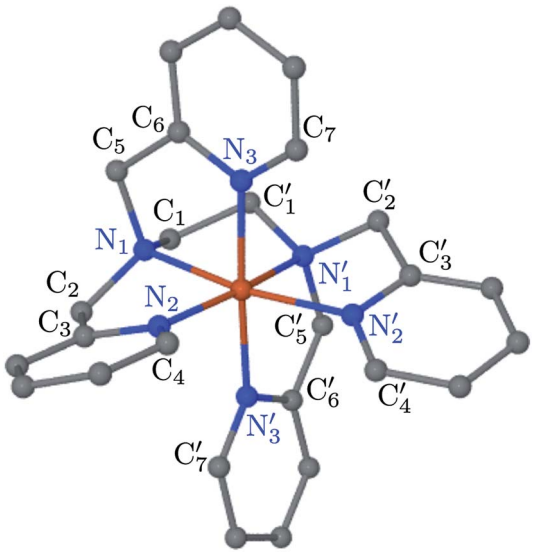

Fig. 2 Average solution structure of LS $[Fe(tpen)]^{2+}$ of C_1 symmetry showing the atom labeling used. In the ideal C_2 symmetry, the atoms X_i and $X_i^{'}$ (X = N and i = {1, 2, 3}, or X = C and i = {1, …, 7}) are interchanged by the C_2 operation.

atoms were described with Goedecker–Teter–Hutter pseudopotentials,[69–71] while their valence states were described with the Gaussian-type MOLOPT[72] DZVP-MOLOPT-SR-GTH basis set of double-zeta polarized quality from the CP2K package. The electron density was expanded in a planewave basis set using a planewave cutoff of 800 Ry and a relative density cutoff of 50 Ry was used. The self-consistent-field calculations were run restricted for the LS state and unrestricted for the HS state. A timestep of 0.5 fs was employed for the integration of the equations of motion. Starting from the initial LS (resp., HS) configuration, the system was equilibrated in the LS (resp., HS) state for 10 ps at constant temperature (T = 310 K). The temperature was controlled by putting a Nosé–Hoover thermostat chain[73] on each ionic degree of freedom (massive thermostating). Thermostating was kept on during the production runs, and the trajectories were recorded every 5 steps (*i.e.*, every 2.5 fs). The lengths of the recorded LS and HS trajectories are Θ_{LS} = 72.0825 ps and Θ_{HS} = 69.0175 ps, respectively.

2.3 Dipole moments and infrared spectra

For the calculations of the dipole moments of the constituents of the solution, the charge distribution was decomposed in terms of maximally-localized Wannier functions (MLWFs).[74] Because of the significant computational cost of the localization procedure, the decomposition was done on the fly with the CP2K program[68] every 10 steps (*i.e.*, every 5.0 fs) only and for the last Θ_{LS}^{W} = 25.3275 ps (resp., Θ_{HS}^{W} = 26.2625 ps) of the simulation in the LS (resp., HS) state, during which the Wannier function centers (WFCs) were recorded. Denoting $\{\mathbf{r}_{i_M}\}$, the WFCs of a molecule M, its dipole moment reads

$$\boldsymbol{\mu}_M = -ze\sum_{i_M}\mathbf{r}_{i_M} + e\sum_{I_M}Z_{I_M}\mathbf{R}_{I_M}, \quad (1)$$

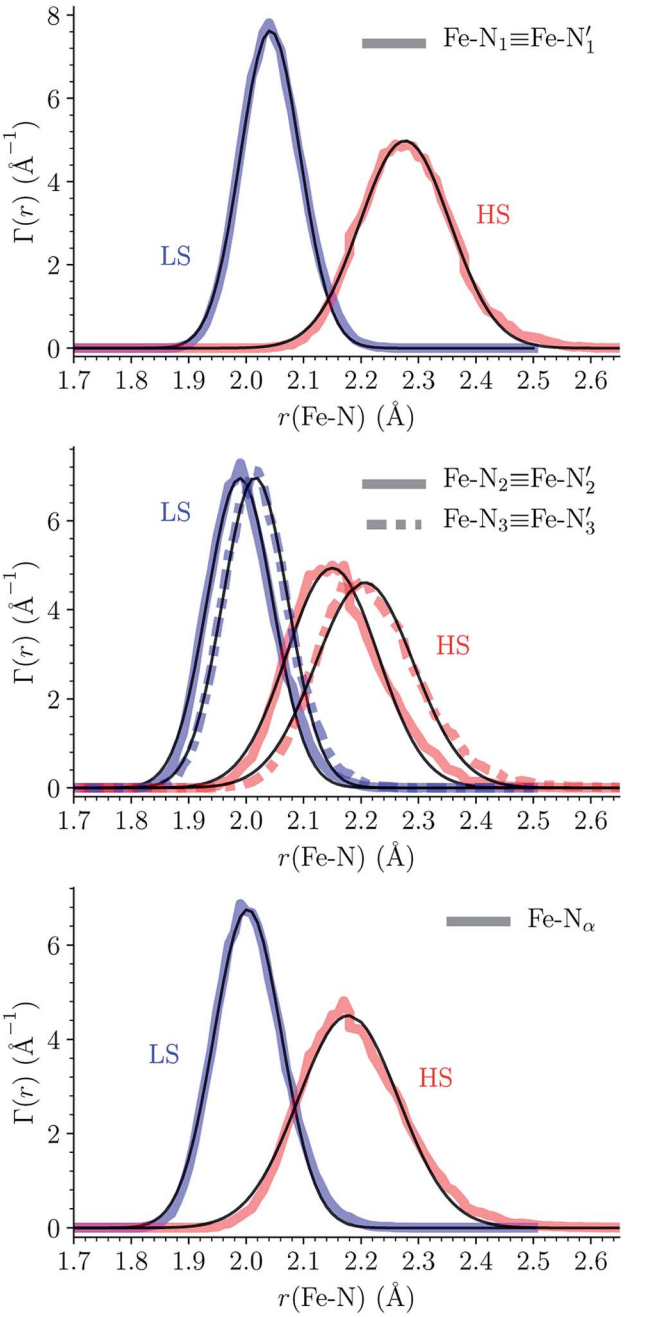

Fig. 3 Distribution functions of the Fe–N bond lengths for $[Fe(tpen)]^{2+}$ in acetonitrile and in the LS and HS states (thick solid or dashed lines). N_α designates the pyridyl nitrogen atoms N_i and $N_i^{'}$ (i = 2, 3). The fits of the data with Gaussians are also shown (black lines).

where z = 2 and z = 1 for spin-restricted and spin-unrestricted calculations, respectively; $\mathbf{R}_{I_M}$ is the position of the "I_M"-th nucleus of M, and Z_{I_M} is its charge. The program Travis[75,76] was used to determine the dipole moments, taking the centers of mass of charged molecules as their dipole reference points, and to calculate the wavenumber-dependent IR molar absorption coefficient according to:[77]

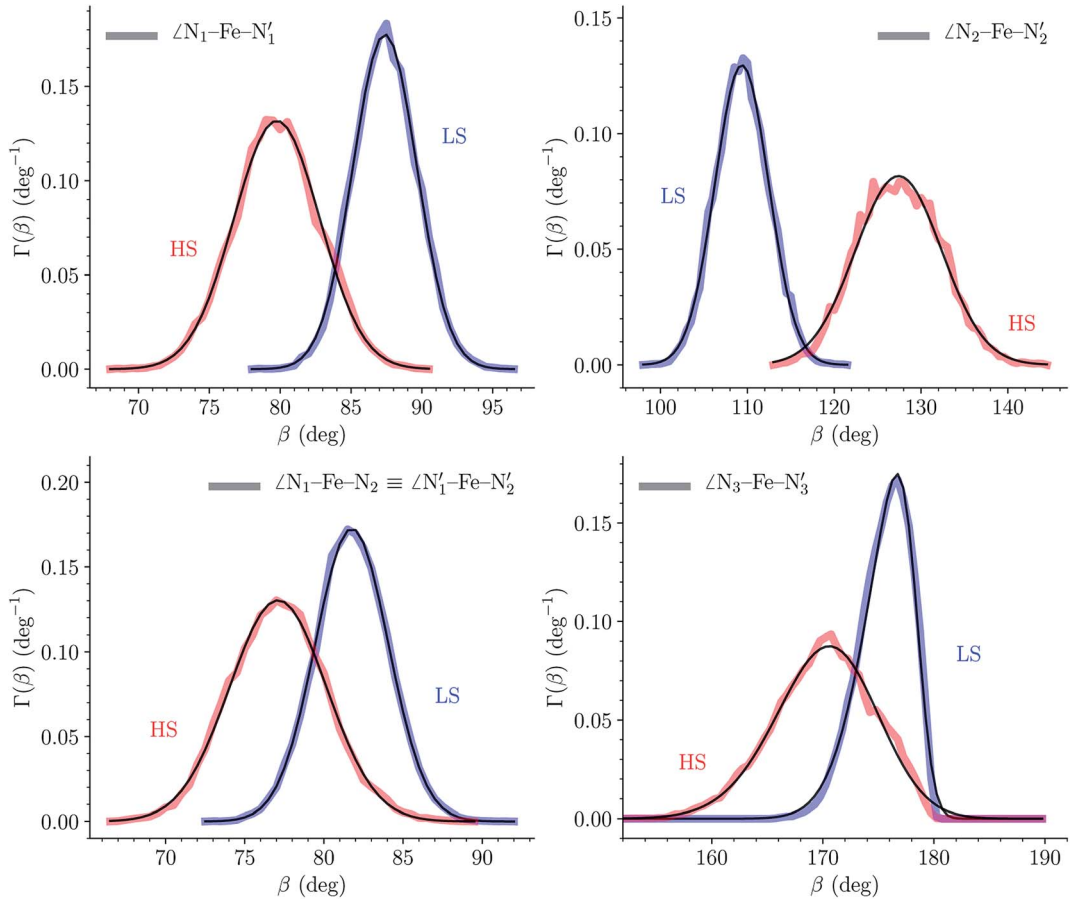

Fig. 4 Distribution functions of the ∠N–Fe–N angles for $[Fe(tpen)]^{2+}$ in acetonitrile and in the LS and HS (thick solid lines). The fits of the data are also shown (black lines): all data were fitted with Gaussians except for the $\angle N_3eFeN_3'$ angle whose distributions were fitted with skewed Gaussians.

$$\varepsilon(\bar{\nu}) = \frac{N_A}{12\varepsilon_0 c k_B T}\int_{-\infty}^{+\infty}\langle\dot{\boldsymbol{\mu}}(\tau)\dot{\boldsymbol{\mu}}(t+\tau)\rangle_\tau \exp(-i2\pi c\bar{\nu}t)dt, \quad (2)$$

where $\bar{\nu}$ is the wavenumber of the incident light, N_A is the Avogadro number, c is the speed of light in vacuum, ε_0 is the vacuum permittivity, k_B is the Boltzmann constant, T is the average simulation temperature, i the imaginary unit, τ and t are time variables, $\dot{\boldsymbol{\mu}}$ is the time derivative of the dipole moment $\boldsymbol{\mu}$, and $\langle\dot{\boldsymbol{\mu}}(\tau)\dot{\boldsymbol{\mu}}(t+\tau)\rangle_\tau$ is the autocorrelation function (ACF) of $\dot{\boldsymbol{\mu}}$ whose Fourier transform is actually taken. The WFC trajectories being recorded every 5 fs, the IR spectra were computed for wavenumbers up to $\nu_{max}^{IR} = 2500\ cm^{-1}$.

2.4 Additional analyses and visualization

The average LS and HS solution structures of $[Fe(tpen)]^{2+}$ and the distribution functions of selected structural parameters were calculated using utilities from the GROMACS program package.[55,56] Radial distributions functions and associated running coordination numbers were computed with the Travis program,[75,76,78] which was also used for the calculations of spatial distribution functions and combined distribution functions. Molecular visualizations were created with the VMD[79,80] and the Jmol[81–83] programs. Curves were plotted using the Matplotlib program package.[84]

3 Results and discussion

3.1 Structural properties

3.1.1 LS and HS structures of $[Fe(tpen)]^{2+}$ in acetonitrile. The LS and HS structures of $[Fe(tpen)]^{2+}$ in ACN have been characterized by calculating in both spin states the distributions of the structural parameters which help describe the arrangement of the tpen ligand around the Fe(II) ion. This includes first parameters associated with the description of the FeN_6 first coordination sphere: namely, the length of the bonds between the Fe and the aminyl N (N_{aminyl}) atoms $Fe-N_1Fe{\equiv}N_1'$; the length of the bonds between the Fe and the pyridyl N ($N_{pyridyl}$) atoms $Fe-N_2Fe{\equiv}N_2'$, the fitting plane to the N_i and N_i' atoms ($i = 1, 2$) defining the equatorial plane of an idealized tetragonal coordination sphere; the bonds between the Fe and the axial $N_{pyridyl}$ atoms $Fe-N_3Fe{\equiv}N_3'$; and the Fe–N bond angles $\angle N_1{-}Fe{-}N_1'$, $\angle N_2{-}Fe{-}N_2'$, $\angle N_1{-}Fe{-}N_2{\equiv}\angle N_1'{-}Fe{-}N_2'$, and $\angle N_3{-}Fe{-}N_3'$ (see Fig. 2 for the atom labeling used). From the experimental point of view, the recent high-resolution TXAS study by Canton *et al.*[37] allowed to distinguish between the Fe–N bonds involving the N_{aminyl} atoms (N_1 and N_1') and those involving the $N_{pyridyl}$ atoms (N_i and N_i' with $i = 2, 3$). However such a distinction could not be made

Table 1 Averages ($\bar{X}$) and standard deviations ($\sigma(X)$) of selected structural parameters characterizing the LS and HS solution structures of $[Fe(tpen)]^{2+}$ in acetonitrile: results of the fit of the parameter distributions using Gaussian distribution functions, except for the $\angle N_3{-}Fe{-}N_3'$ angle whose distributions were fitted with skewed Gaussian distribution functions (see Text). λ is the skewness parameter entering the definition of the skewed Gaussian distributions. Available experimental data are also shown[a]

		AIMD			Exp.
		$\bar{X}$	$\sigma(X)$	λ	In ACN[b]
$Fe{-}N_1 \equiv Fe{-}N_1'$ (Å)	LS	2.042	0.052		2.02(2)
	HS	2.277	0.078		2.26(2)
$Fe{-}N_2 \equiv Fe{-}N_2'$ (Å)	LS	1.989	0.057		—
	HS	2.150	0.079		—
$Fe{-}N_3 \equiv Fe{-}N_3'$ (Å)	LS	2.016	0.057		—
	HS	2.206	0.085		—
$Fe{-}N_\alpha$ (Å)	LS	2.003	0.059		1.98(2)
	HS	2.178	0.088		2.15(2)
$\angle N_1{-}Fe{-}N_1'$ (deg)	LS	87.4	2.3		
	HS	79.8	3.0		
$\angle N_2{-}Fe{-}N_2'$ (deg)	LS	109.4	3.1		
	HS	127.4	5.0		
$\angle N_1{-}Fe{-}N_2 \equiv \angle N_1'{-}Fe{-}N_2'$ (deg)	LS	81.8	2.3		
	HS	77.1	3.1		
$\angle N_3{-}Fe{-}N_3'$ (deg)	LS	178.4	3.8	−3.2	
	HS	173.6	5.8	−1.1	
Π_1 (deg)	LS	88.9	6.7		
	HS	93.7	8.3		
Π_2 (deg)	LS	144.7	7.3		
	HS	150.6	11.4		

[a] N_α designates the pyridyl nitrogen atoms N_i and N_i' ($i = 2, 3$); Π_1 is the angle between the three-atom planes $\mathscr{P}(C_6, N_3, C_7)$ and $\mathscr{P}(C_6', N_3', C_7')$ respectively defined by the basis vectors $(\overrightarrow{N_3C_6}, \overrightarrow{N_3C_7})$ and $(\overrightarrow{N_3'C_6'}, \overrightarrow{N_3'C_7'})$, and Π_2 is the angle between the three-atom planes $\mathscr{P}(C_3, N_2, C_4)$ and $\mathscr{P}(C_3', N_2', C_4')$ .defined by the basis vectors $(\overrightarrow{N_2C_3}, \overrightarrow{N_2C_4})$ and $(\overrightarrow{N_2'C_3'}, \overrightarrow{N_2'C_4'})$, respectively. [b] Ref. 37.

between these latter ones. Hence, to allow a direct comparison with the experimental results, we have also calculated the distribution of the length of the bonds between the Fe and the four $N_{pyridyl}$ atoms, thereafter also denoted N_α.

The distributions of the Fe–N bond lengths are plotted in Fig. 3. They are quite broad for $[Fe(tpen)]^{2+}$ in the LS state, which reflects the large thermal fluctuations undergone by the solvated complex. They become broader and exhibit a ~0.2 Å shift towards longer bond lengths for HS $[Fe(tpen)]^{2+}$, as a consequence of the weakening of the Fe–N bonds and the accompanying increase in the thermal fluctuations. The LS → HS change of states indeed involves the promotion of two electrons from the mostly nonbonding metallic Fe(3d) orbitals of octahedral t_{2g} parentage into the antibonding metallic Fe(3d) orbitals of octahedral e_g parentage. One also notes that in either spin state, the distributions of the $Fe{-}N_2 \equiv Fe{-}N_2'$ and $Fe{-}N_3 \equiv Fe{-}N_3'$ bonds lengths strongly overlap. This explains why it proves difficult to discriminate experimentally between the two types of $Fe{-}N_{pyridyl}$ bond lengths.[37]

The distributions of the selected Fe–N bond angles are plotted in Fig. 4. As observed for the distribution of the Fe–N bond lengths, these distributions are broad for LS $[Fe(tpen)]^{2+}$ and become broader for HS $[Fe(tpen)]^{2+}$ because of the increased thermal fluctuations accompanying the weakening of the Fe–N bonds. For LS $[Fe(tpen)]^{2+}$, the $\angle N_3{-}Fe{-}N_3'$ angle distribution function is strongly asymmetric: it is peaked

Table 2 Averages ($\bar{X}$) and standard deviations ($\sigma(X)$) of selected Fe–C distances characterizing the LS and HS solution structures of $[Fe(tpen)]^{2+}$ in acetonitrile: results of the fit of the parameter distributions using Gaussians. Available experimental data are also shown[a]

		AIMD		Exp.
		$\bar{X}$	$\sigma(X)$	In ACN[b]
$Fe{-}C_1 \equiv Fe{-}C_1'$ (Å)	LS	2.845	0.057	2.82(3)
	HS	3.071	0.093	2.98(2)
$Fe{-}C_2 \equiv Fe{-}C_2'$ (Å)	LS	2.826	0.054	
	HS	2.999	0.086	
$Fe{-}C_3 \equiv Fe{-}C_3'$ (Å)	LS	2.820	0.053	
	HS	2.981	0.078	
$Fe{-}C_4 \equiv Fe{-}C_4'$ (Å)	LS	3.022	0.073	
	HS	3.132	0.105	
$Fe{-}C_5 \equiv Fe{-}C_5'$ (Å)	LS	2.944	0.059	
	HS	3.113	0.094	
$Fe{-}C_6 \equiv Fe{-}C_6'$ (Å)	LS	2.878	0.053	
	HS	3.045	0.088	
$Fe{-}C_7 \equiv Fe{-}C_7'$ (Å)	LS	3.022	0.072	
	HS	3.183	0.102	
$Fe{-}C_\beta$ (Å)	LS	2.850	0.062	2.87(3)
	HS	3.011	0.090	3.04(2)
$Fe{-}C_\gamma$ (Å)	LS	2.886	0.090	2.93(3)
	HS	3.056	0.110	3.10(2)
$Fe{-}C_\delta$ (Å)	LS	3.022	0.073	3.03(3)
	HS	3.158	0.107	3.20(2)

[a] C_β designates the carbon atoms C_i and C_i' ($i = 3, 6$), C_γ the carbon atoms C_i and C_i' ($i = 2, 5$), and C_δ the atoms C_i and C_i' ($i = 4, 7$). [b] Ref. 37.

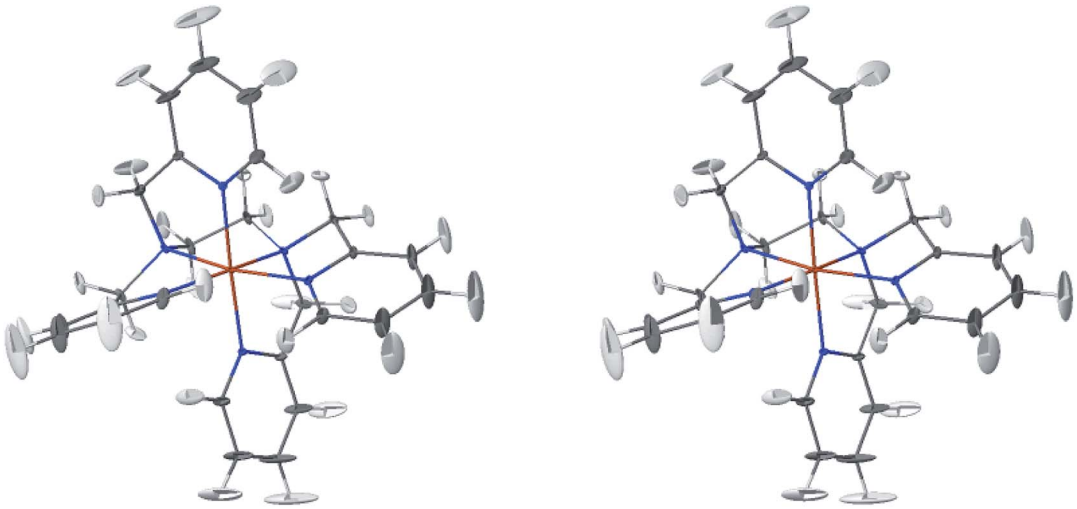

Fig. 5 Stereoscopic view of the average structures of LS $[Fe(tpen)]^{2+}$ in acetonitrile with the 50% probability ellipsoids.

around 178 deg, smoothly decreasing towards smaller angle values while abruptly vanishing towards higher values. This is due to the chelating coordination motif of the tpen hexadentate ligand which prevents this angle from taking values higher than 178 deg. Note that, although it is less pronounced, the asymmetry of the $\angle N_3{-}Fe{-}N_3^{'}$ angle distribution is maintained for HS $[Fe(tpen)]^{2+}$. Upon the LS $\rightarrow$ HS change of states, the $\angle N_1{-}Fe{-}N_1^{'}$, $\angle N_1{-}Fe{-}N_2 \equiv \angle N_1^{'}eFe{-}N_2^{'}$ and $\angle N_3{-}Fe{-}N_3^{'}$ angles decrease by $\sim$5 deg to $\sim$7 deg while the $\angle N_2{-}Fe{-}N_2^{'}$ angle increases by $\sim$17 deg: this reflects the rearrangement of the tpen ligand around the Fe atom entailed by the lengthening of the Fe–N bonds.

The Fe–N distances distributions could be satisfactorily fitted using Gaussian distributions functions (Fig. 3). They exhibit a slight departure from an ideal Gaussian distribution, which is more marked for $[Fe(tpen)]^{2+}$ in the HS state. These slight deviations from Gaussian distributions can be ascribed to the anharmonicity of the motion of the complex on its free energy surface, especially along the Fe–N distance coordinates.[43,46] The distributions of the $\angle$N–Fe–N angles could all be well fitted with Gaussian distributions, except those of the $\angle N_3{-}Fe{-}N_3^{'}$ angle for which skewed Gaussian distributions were used so as to take into account the asymmetry of its distributions (Fig. 4).

Table 1 summarizes the averages and standard deviations obtained from the fits of the Fe–N bond lengths. The $Fe{-}N_1 \equiv Fe{-}N_1^{'} \equiv Fe{-}N_{aminyl}$ bond lengths are predicted to increase from 2.042 Å to 2.277 Å on going from the LS to the HS state, and the $Fe{-}N_{\alpha} \equiv Fe{-}N_{pyridyl}$ bond lengths are predicted to increase from 2.003 Å to 2.178 Å. These results are in excellent agreement with the experimental ones[85] also reported in Table 1. This attests for the high accuracy of the structural information gained from the AIMD simulations. This is the case for the distinction achieved between the axial and equatorial $Fe{-}N_{pyridyl}$ bond lengths: the LS to HS change of states is thus found to be accompanied by the increase of the $Fe{-}N_2 \equiv Fe{-}N_2^{'}$ bond

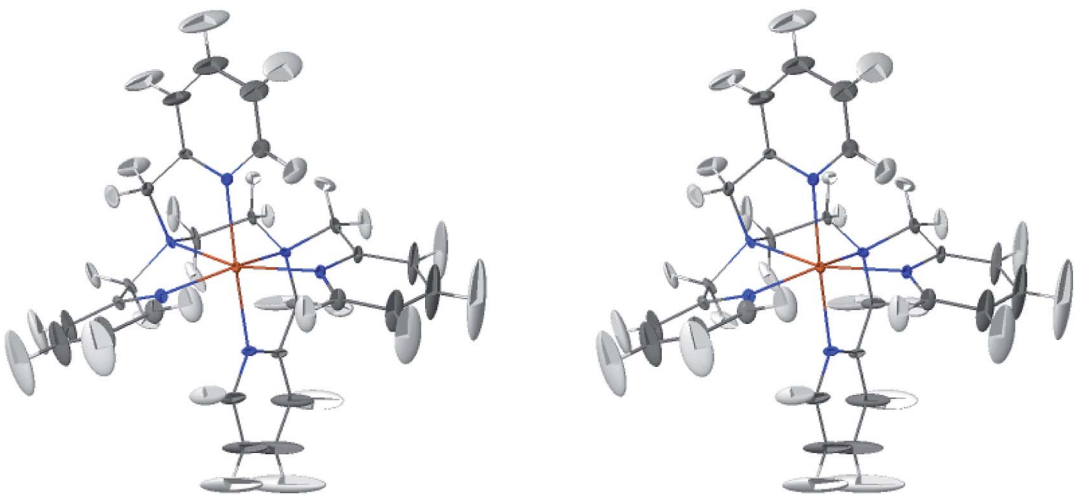

Fig. 6 Stereoscopic view of the average structures of HS $[Fe(tpen)]^{2+}$ in acetonitrile with the 50% probability ellipsoids.

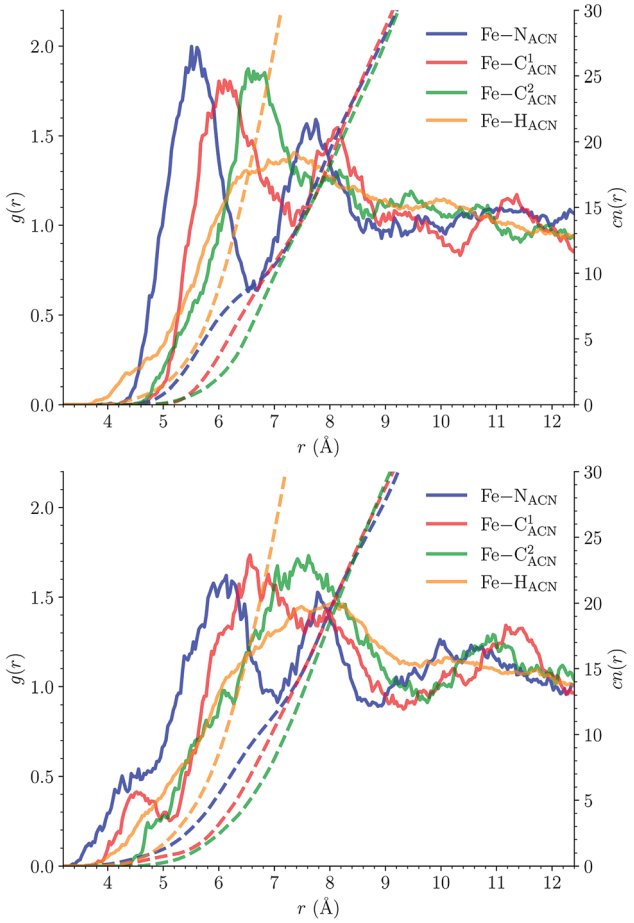

Fig. 7 Solvation structure of $[Fe(tpen)]^{2+}$ in the LS (top) and in the HS state (bottom): radial distribution functions $g(r)$ of the acetonitrile nitrogen (N_{ACN}), carbon ($N_{ACN}{\equiv}C^1_{ACN}{-}C^2_{ACN}$) and hydrogen ($H_{ACN}$) atoms with respect to the Fe atom (solid lines, left y-axis), and running coordination numbers $cn(r)$ (dashed lines, left y-axis).

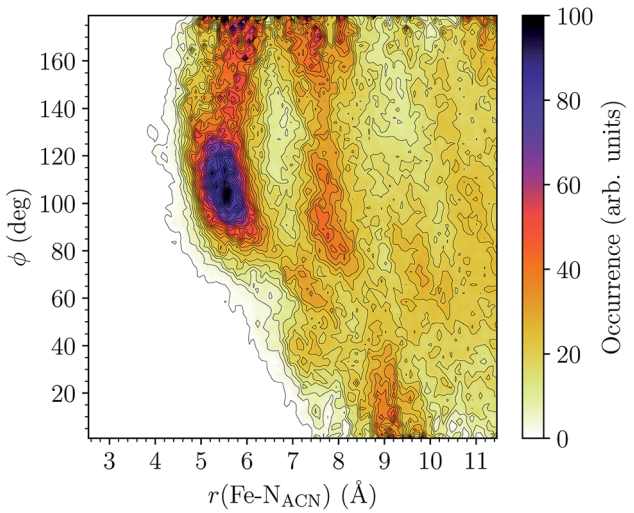

Fig. 8 Combined $r(Fe{-}N_{ACN})/\phi$ radial/angular distribution function for $[Fe(tpen)]^{2+}$ in the LS state; ϕ is the angle $\angle FeN_{ACN}C^1_{ACN}$ where N_{ACN} and C^1_{ACN} are the atoms of the nitrile group belonging to the ACN molecule observed at a distance r from the Fe atom.

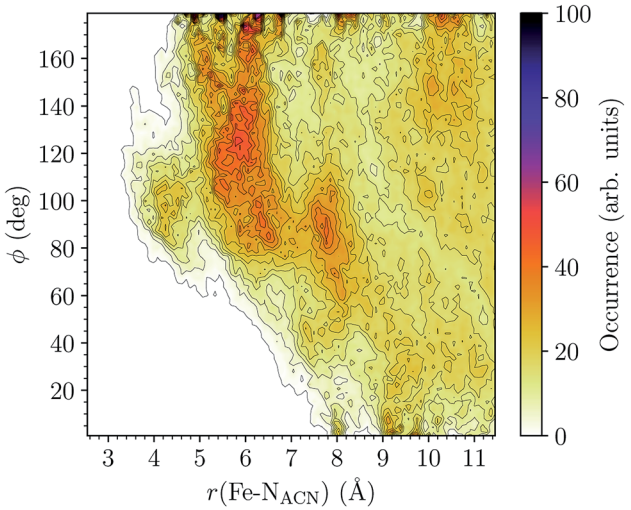

Fig. 9 Combined $r(Fe{-}N_{ACN})/\phi$ radial/angular distribution function for $[Fe(tpen)]^{2+}$ in the HS state; ϕ is the angle $\angle FeN_{ACN}C^1_{ACN}$ where N_{ACN} and C^1_{ACN} are the atoms of the nitrile group belonging to the ACN molecule observed at a distance r from the Fe atom.

length from 1.989 Å to 2.150 Å and of the $Fe{-}N_3{\equiv}Fe{-}N_3'$ bond length from 2.016 Å to 2.206 Å. Consequently, the $Fe{-}N_{aminyl}$ bonds show the largest lengthening (+0.235 Å) upon the LS → HS transition, followed by the axial $Fe{-}N_{pyridyl}$ bonds (+0.190 Å) and then by equatorial $Fe{-}N_{pyridyl}$ bonds (+0.161 Å).

Table 1 also summarizes the averages and standard deviations obtained from the fits of the selected ∠N–Fe–N angles. For the $\angle N_3{-}Fe{-}N_3'$ angle whose distributions in the LS and HS states have been fitted with skewed Gaussian distribution functions, the values found for the skewness parameter λ are also reported: $\lambda < 0$ as expected for left-skewed distributions and its magnitude decreases from 3.2 to 1.1 on going from the LS to the HS state as a consequence of the reduced asymmetry of the distribution.

The angle Π_1 between the three-atom planes $\mathscr{P}(C_6,\ N_3,\ C_7)$ and $\mathscr{P}(C_6',\ N_3',\ C_7')$ and the angle Π_2 between the three-atom planes $\mathscr{P}(C_3,\ N_2,\ C_4)$ and $\mathscr{P}(C_3',\ N_2',\ C_4')$ have been introduced to describe the relative orientations of the axial pyridine rings and of the equatorial ones, respectively. Their LS and HS distributions could be satisfactorily fitted with Gaussian distribution functions, as shown in the ESI (Fig. S1†). The averages and standard deviations obtained from the fits for Π_1 and Π_2 are given in Table 1. Π_1 is found to increase from 88.9 deg to 93.7 deg on passing from the LS to the HS state, and Π_2 from 144.7 deg to 150.6 deg. That is, the axial pyridine rings thus tend to remain perpendicular in the two spin states and the twist between the equatorial pyridine rings decreases on passing from the LS to the HS state.

In order to characterize further the arrangement of tpen around the Fe atom beyond the FeN_6 first coordination sphere, the distributions of the $Fe{-}C_i{\equiv}Fe{-}C_i'$ ($i = 1,\ \ldots,\ 7$) bond lengths have been calculated as well as those of the Fe–C_β, Fe–C_γ and Fe–C_δ bond lengths, which, in addition to the $Fe{-}C_1{\equiv}Fe{-}C_1'$ bond length, could be experimentally

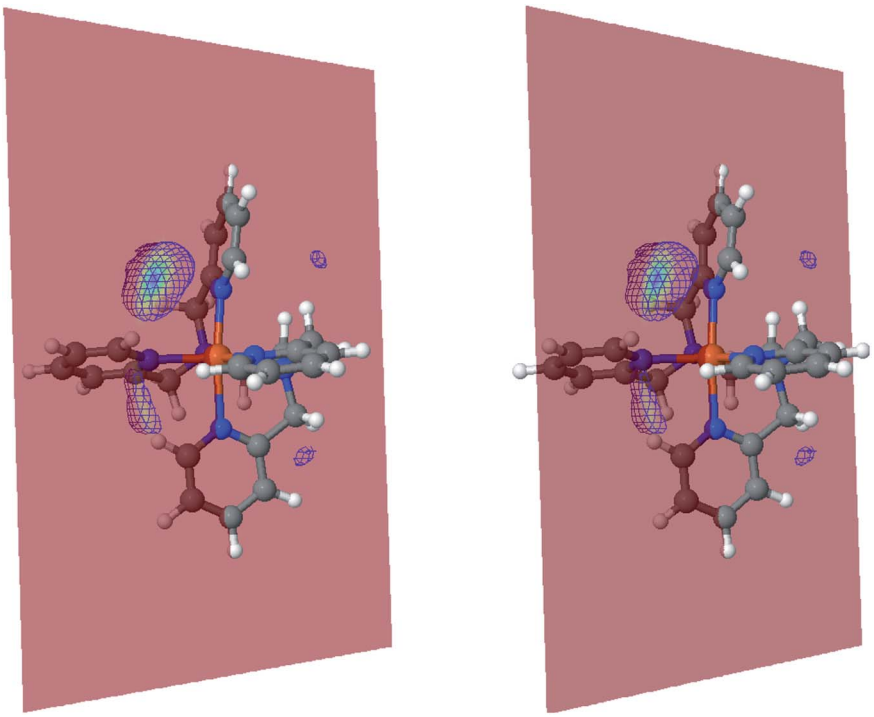

Fig. 10 Stereoscopic view of the spatial distribution function of the N_{ACN} atoms of the ACN molecules entering the inner solvation shell of HS $[Fe(tpen)]^{2+}$: the meshed isosurface corresponds to a particule density of 30 nm^{-3} (density range: 0 to 552 nm^{-3}), and the contour plot is in the plane defined by the N_3 and Fe atoms and by the barycenter of the N_2 and N_2' atoms (see Fig. 2 for the atom labeling scheme).

determined for $[Fe(tpen)]^{2+}$ in ACN.[37] Here, C_β designates the ligand's chemically equivalent C atoms C_i and C_i' ($i = 3, 6$), C_γ the atoms C_i and C_i' ($i = 2, 5$), and C_δ the atoms C_i and C_i' ($i = 4, 7$). These distributions have been satisfactorily fitted with Gaussian functions (Fig. S2 and S3, ESI†). The averages and standard values of the Fe–C bond lengths thus obtained are summarized in Table 2 along with the available experimental data, with which a good agreement is also observed.

The LS and HS average solution structures of $[Fe(tpen)]^{2+}$ have been calculated and stereoscopic views of them are shown in Fig. 5 and 6, respectively. The 50% probability ellipsoids associated with the thermal fluctuations of the atoms about their average positions are also represented. The inspection of each figure shows that, in either spin state, the thermal fluctuations increase on moving away from the metal atom and hence with the exposure of the atoms to the solvent, the smallest atomic displacements being for the atoms which belong to five-membered chelate rings. The comparison of the two figures shows that the LS → HS change of states is accompanied by an increase of the atomic disorder as measured by the volumes of the ellipsoids.

The thermal ellipsoids of the atoms of the tpen ligand are strongly anisotropic. Such a privileged directionality of the atomic displacements can be explained by the strength and directionality of the Fe–N bonds and also by the rigidity of the hexadentate tpen ligand, be it the rigidity of pyridyl moities or the one which results from its chelating coordination motif. For the atoms belonging to the pyridine rings of tpen, the major principal axes of their thermal ellipsoids tend to be perpendicular to the average planes of the rigid pyridine rings: this follows from the rigidity of the rings and from the strong and directional character of the Fe–N bonds which hinder the atomic motion along directions parallel to the average planes of the pyridine rings.[46] As for the CH_2 groups of tpen, the major principal axes of the thermal ellipsoids associated with the atomic displacements tend to be located in the planes defined by the average positions of their atoms. This can be ascribed to the fact that the out-of-plane motions of their atoms are hindered by the belonging of their C atoms to five-membered chelate rings whose conformational flexibility is somehow limited by the requirement to maintain the Fe(II)-tpen bonding optimal.

3.1.2 Solvation structure of $[Fe(tpen)]^{2+}$. The solvation structure of $[Fe(tpen)]^{2+}$ in the LS and HS states has been characterized by determining the radial distribution functions (RDFs) of the acetonitrile nitrogen (N_{ACN}), carbon ($N_{ACN}{\equiv}C^1_{ACN}$–C^2_{ACN}) and hydrogen (H_{ACN}) atoms with respect to the Fe atom. They are plotted in Fig. 7 along with the associated running coordinations numbers.

LS $[Fe(tpen)]^{2+}$. For $[Fe(tpen)]^{2+}$ in the LS state, the Fe–N_{ACN}, Fe–C^1_{ACN} and Fe–C^2_{ACN} RDFs exhibit each a first well-resolved peak at ≈5.6 Å, ≈6.1 Å and ≈6.7 Å, respectively, with a minimum at ≈6.6 Å, ≈7.3 Å and ≈7.7 Å, respectively. The presence and ordering of these peaks indicates that the first solvation shell of LS $[Fe(tpen)]^{2+}$ is structured, and that the ACN molecules present in this solvation shell tend to be oriented with their N_{ACN} heads pointing toward the Fe atom. The fact that the 0.5–0.6 Å distance between the peaks does not match

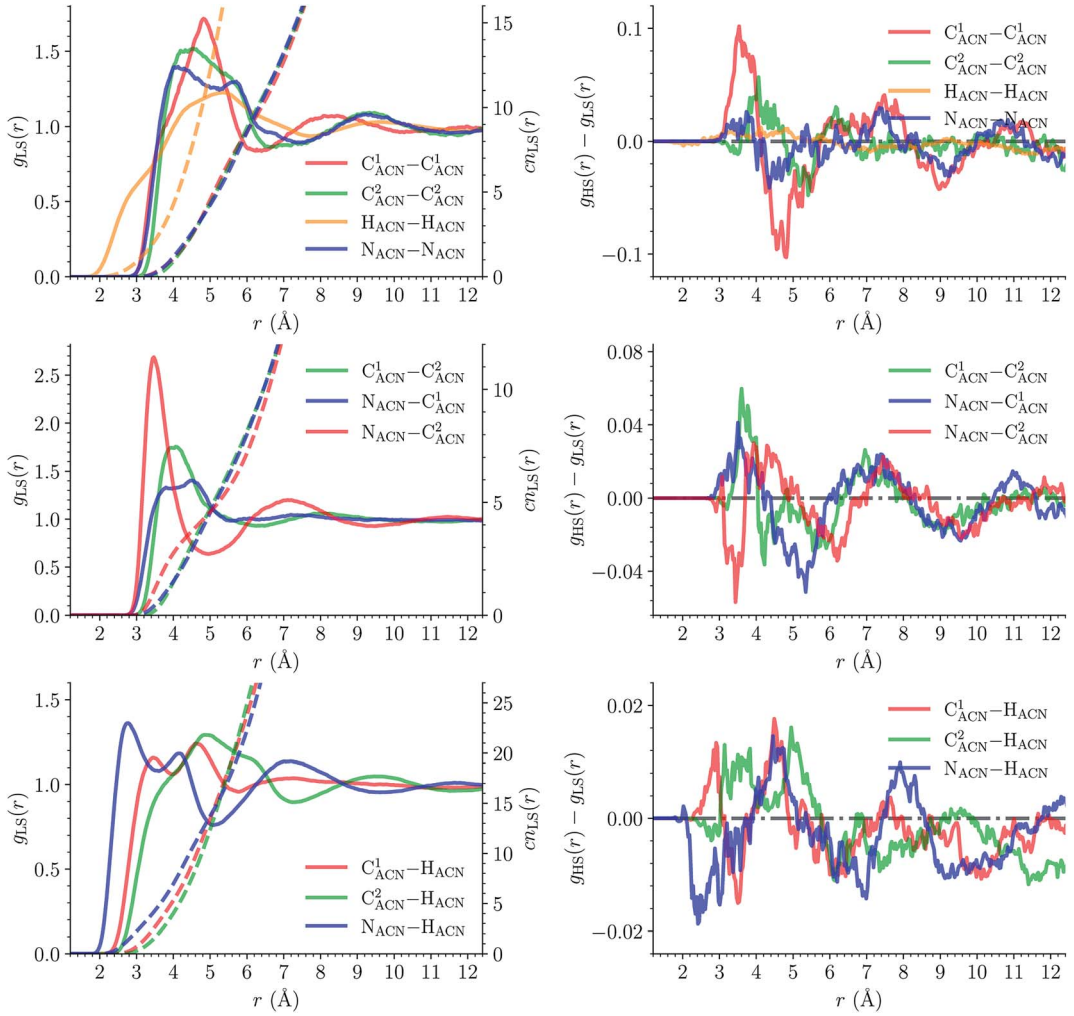

Fig. 11 Structure of the acetonitrile solvent state (atom labeling: $N_{ACN}{\equiv}C^1_{ACN}{-}C^2_{ACN}(H_{ACN})_3$): (left) intermolecular radial distribution functions $g(r)$ (solid lines, left y-axis) and running coordination numbers $cn(r)$ (dashed lines, left y-axis) for $[Fe(tpen)]^{2+}$ in the LS state; (right) differences between the HS and LS radial distribution functions.

the interactomic distances in the ACN molecule suggests that there is no colinearity between (i) the line passing through the Fe atom and the N_{ACN} atom of the observed ACN molecule and (ii) the ACN molecular axis simply taken as the one defined by its nitrile group. This is supported by the plot in Fig. 8 of the combined $r(Fe{-}N_{ACN})/\phi$ radial/angular distribution function (CDF): ϕ is the angle $\angle FeN_{ACN}C^1_{ACN}$ where N_{ACN} and C^1_{ACN} are the atoms of the nitrile group belonging to the ACN molecule observed at a distance r from the Fe atom. For the ACN molecules in the first solvation shell ($r(Fe{-}N_{ACN}) \leq 6.6$ Å), one indeed notes in Fig. 8 that the $r(Fe{-}N_{ACN})/\phi$ CDF exhibits a broad and tall peak culminating at $r \approx 5.6$ Å $\phi \approx 100$ deg and covering the area delimited by 5.0 Å $\leq r \leq$ 6.1 Å and 90 deg $\lesssim \phi \lesssim$ 120 deg. Besides these dominantly preferred orientations, ACN molecules in the first solvation shell adopt orientations with $\phi >$ 120 deg. For 6.6 Å $\lesssim r \lesssim$ 8.5 Å, that is, for ACN molecules in the second solvation shell (see below), the preferred orientations correspond to 70 deg $\leq \phi \leq$ 180 deg. One also observes a massif covering the area delimited by 8.6 Å $\leq r \leq$ 10.0 Å and 0 deg $\lesssim \phi \lesssim$ 40 deg. Beyond $r =$ 10 Å, in the bulk, no real preferential ϕ orientation is observed.

One notes in Fig. 7 that the Fe–N_{ACN} and Fe–C^1_{ACN} RDFs present a second peak at ≈7.7 Å and ≈8.1 Å, respectively, with a minimum at ∼8.7 Å for both RDFs. These features indicate the presence of a second solvation shell, which, however, is not as structured as the first solvation shell in that the Fe–C^2_{ACN} RDF does not exhibit a well-defined second peak. The Fe–H_{ACN} RDF shows a main broad peak at ≈7.3 Å with a shallow minimum at ∼9.3 Å. It takes non-vanishing values at distances shorter than the other RDFs because the ACN H atoms can go closer to the Fe atom than the ACN N and C atoms of larger van der Waals radii. The number of ACN molecules in the first solvation shell of LS $[Fe(tpen)]^{2+}$, namely its solvation number, is given by the value of the Fe–N_{ACN} running coordination number at the position of the minimum associated with the first peak of the Fe–N_{ACN} RDF. It thus amounts to ≈9.2. As illustrated by the snapshot from the HS trajectory (Fig. 1), the ACN molecules of the first solvation enter the grooves defined by the coordinating tpen ligand.

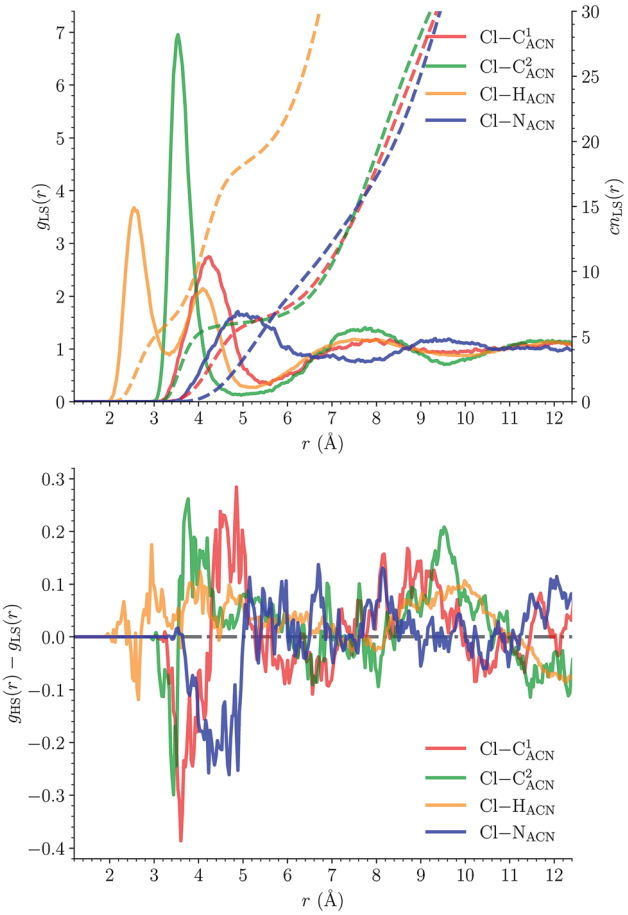

Fig. 12 Solvation structure of Cl^- in acetonitrile (atom labeling: $N_{ACN}{\equiv}C^1_{ACN}{-}C^2_{ACN}(H_{ACN})_3$): (top) radial distribution functions $g(r)$ (solid lines, left y-axis) and running coordination numbers $cn(r)$ (dashed lines, left y-axis) for $[Fe(tpen)]^{2+}$ in the LS state; (bottom) differences between the HS and LS radial distribution functions.

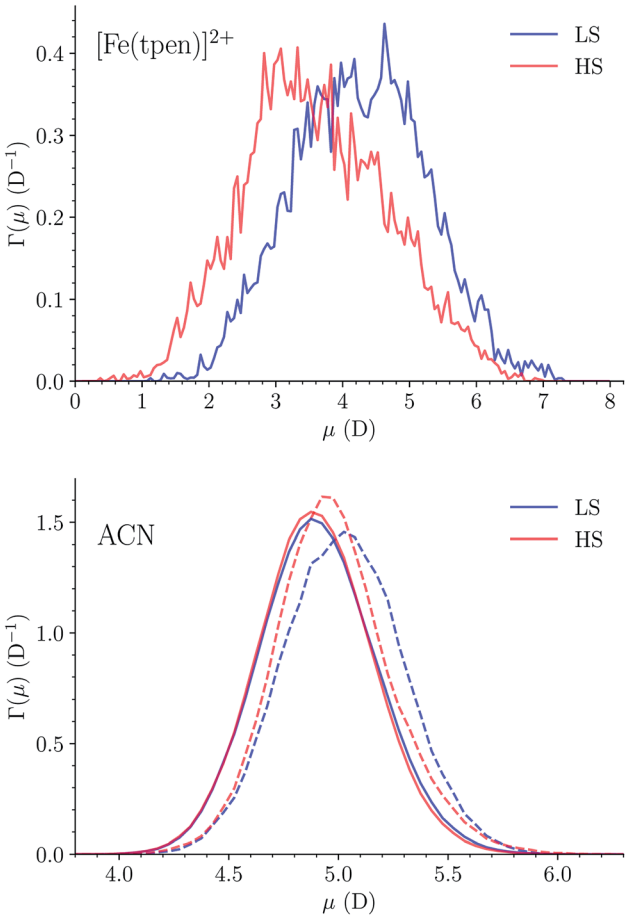

Fig. 13 Dipole distribution functions of (top) $[Fe(tpen)]^{2+}$ in the LS and in the HS state, and of (bottom) the ACN molecules in (r(Fe–N_{ACN}) ≤ $r_{1,min}$, dashed lines) and beyond (r(Fe–N_{ACN}) > $r_{1,min}$, solid lines) the first solvation shell of $[Fe(tpen)]^{2+}$ in the LS and in the HS state ($r_{1,min}|_{LS}$ = 6.6 Å, $r_{1,min}|_{HS}$ = 7.1 Å).

HS [Fe(tpen)]$^{2+}$. Upon the LS → HS change of states, the Fe–N_{ACN}, Fe–C^1_{ACN} and Fe–C^2_{ACN} RDFs are shifted to lower distances (Fig. 7): that is, the lengthening of the Fe–N bonds and the accompanying structural rearrangement of the tpen ligand allow the ACN molecules to go closer to the Fe atom. The Fe–N_{ACN} and Fe–C^1_{ACN} RDFs present also a peak at ≈4.4 Å and ≈4.5 Å, respectively, with a minimum at ≈4.7 Å and ≈5.1 Å, respectively, while the Fe–CC^2_{ACN} RDF shows a shoulder centered at ≈5.0 Å. This indicates the formation of an inner solvation shell with ≈0.8 ACN molecule. The main peaks of the Fe–N_{ACN}, Fe–C^1_{ACN} and Fe–C^2_{ACN} are broader than in the LS state with their maxima displaced to longer distances at ≈6.1 Å, ≈6.6 Å and ≈7.4 Å, respectively, and their minima at ≈7.1 Å, ≈7.6 Å and ≈9.8 Å, respectively. The broad peak of the Fe–H_{ACN} RDF is also displaced to longer distance, at ≈8.0 Å, with its shallow minimum moved to ≈9.5 Å. Thus, on passing from the LS to the HS state, the first solvation shell of $[Fe(tpen)]^{2+}$ becomes less structured. Fig. 9 shows the plot of the r(Fe–N_{ACN})/ϕ CDF calculated for the complex in the HS state. The peak at r ≈ 4.2 Å shows that the ≈0.8 ACN molecule entering the inner solvation shell adopts orientations distributed around ϕ ≈ 100 deg, while the massif located at r ≈ 6.0 Å indicates preferred orientations centered about ϕ ≈ 120 deg for the other ACN molecules in the first solvation shell. The solvation number of HS $[Fe(tpen)]^{2+}$ is ≈11.9. It follows that about 3 ACN molecules enter the first solvation shell of $[Fe(tpen)]^{2+}$ upon the LS → HS change of states.

The inner solvation shell of HS $[Fe(tpen)]^{2+}$ has been characterized by calculating the spatial distribution function (SDF) of the N_{ACN} atom belonging to the ACN molecule(s) entering the inner shell. These are the ACN molecules for which r(Fe–N_{ACN}) ≤ 4.7 Å (Fig. S4, ESI†). A stereoscopic view of the SDF is shown in Fig. 10 along with its contour plot in the plane defined by the N_3 and Fe atoms and by the barycenter of the N_2 and N_2' atoms. The inspection of the SDF shows that the ACN molecule in the inner solvation shell is dominantly located in the internal cavity which results from the arrangement of the 4 pyridine rings. The internal cavity can be schematically depicted as the polyhedral cone whose generators pass through the Fe atom and the four H atoms, H_i and H_i', which are respectively attached to the C_i and C_i' (i = 4, 7) of the pyridine rings. The ACN molecule can be located on either side of the equatorial plane defined by the

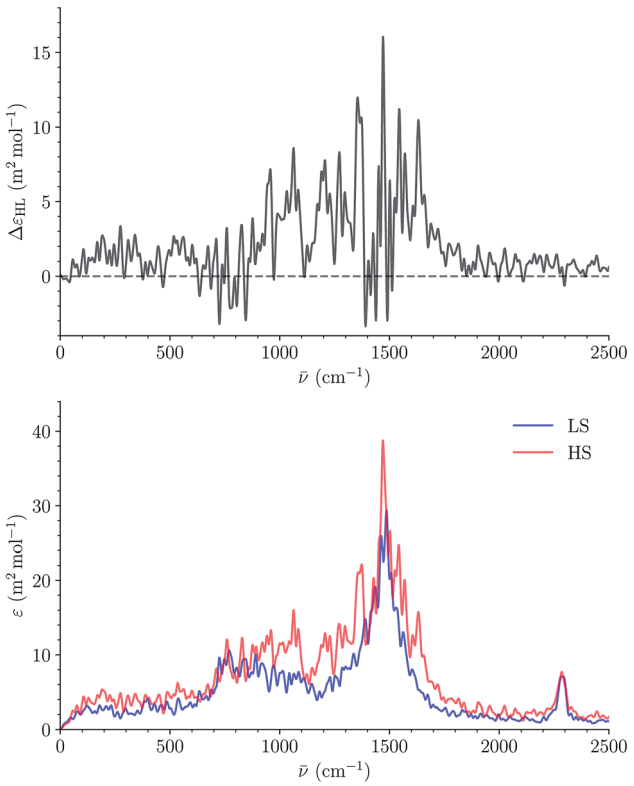

Fig. 14 Calculated LS and HS 310 K IR spectra of $[Fe(tpen)]^{2+}$ in ACN (bottom) and corresponding HS-LS difference curve (top; resolution of the ACFs: 512 time steps).

fitting plane to the N_i and $N_i^{'}$ atoms ($i = 1, 2$). The cavity is not accessible to the solvent molecules in the LS state, its entrance being hindered by the H_i and $H_i^{'}$ ($i = 4, 7$) atoms. Upon the LS → HS change of states, it becomes accessible since these H atoms move away as a results of the lengthening of the Fe–N bonds and to the concomitant large widening of the $\angle N_2{-}Fe{-}N_2^{'}$ bond angle, as anticipated in ref. 37. The fact that this internal cavity can become accessible to molecules as small as ACN in the HS state only probably explains why $[Fe(tpen)]^{2+}$ exhibits a spin-state dependent reactivity towards dioxygen, superoxide or nitric oxide.[52–54] We will elaborate on the entailment of our finding for the chemical reactivity of the complex in the "Conclusion and outlook" Section, after having completed the AIMD characterization of the $[Fe(tpen)]^{2+}$ solution.

3.1.3 Additional structural features of the solution. The different RDFs characterizing the organization of the ACN solvent have all been calculated for $[Fe(tpen)]^{2+}$ in the LS state; they are plotted in Fig. 11. These RDFs have also been calculated for $[Fe(tpen)]^{2+}$ in the HS state (Fig. S6, ESI†) and prove to be similar to those obtained for the LS $[Fe(tpen)]^{2+}$ solution, as attested for by the plot in Fig. 11 of the differences $g_{HS}(r) - g_{LS}(r)$ between the RDFs determined for the complex in the HS ($g_{HS}(r)$) and in the LS ($g_{LS}(r)$) state. The similarity between the RDFs determined for the complex in the two states indicate that the structure of the ACN solvent is not significantly affected by the change of spin states. The calculated RDFs are in very good agreement with those determined for liquid ACN from X-ray and neutron diffraction data by Pothoczki and Puszta using the reverse Monte Carlo method,[86] The C^1_{ACN}–C^1_{ACN}, C^1_{ACN}–N, N_{ACN}–H_{ACN}, N_{ACN}–N_{ACN} RDFs are also in very good agreement with those recently determined for liquid ACN by Sánchez Marcos and coworkers from MD simulations performed using the flexible and polarizable force field which they designed for the accurate description of ACN in the solid, liquid and gas phases.[87] Consequently, the present AIMD simulations allowed to achieve an accurate characterization of the ACN solvent for the $[Fe(tpen)]Cl_2$ solution in the two spin states.

The solvation structure of the Cl^- anions has been characterized in the two spin states by calculating the Cl–X (X = H_{ACN}, N_{ACN}, C^1_{ACN}, C^2_{ACN}) RDFs. Fig. 12 shows the plot of the LS Cl–X RDFs with the associated running coordination numbers, as well as the plot of the differences $g_{HS}(r) - g_{LS}(r)$ between the HS and LS Cl–X RDFs. The relatively small magnitudes of the difference curves indicate a weak dependence of the solvation structure of the anions on the spin state of $[Fe(tpen)]^{2+}$. Longer simulation times would allow for a decrease of the noise in the RDFs and hence for a better signal-to-noise ratio of the $g_{HS}(r) - g_{LS}(r)$ curves whose magnitudes would probably also decrease. The Cl–H_{ACN}, Cl–C^2_{ACN} and Cl–C^1_{ACN} RDFs show well-resolved peaks at ≈2.6 Å, ≈3.5 Å, ≈4.2 Å, respectively, which all three lead to a coordination number of ≈6 (see also Fig. S7, ESI†). That is, for the complex in either spin state, the first solvation shell of Cl^- is very structured and made of 6 H-bonded ACN molecules. Two snapshots from the LS trajectory illustrating the first solvation shell of the Cl^- anions are presented in Fig. S8 (ESI†). During the AIMD simulations, the Cl^- counteranions are found to stay in the vicinity of the $[Fe(tpen)]^{2+}$ complex in either spin state (Fig. S9, ESI†), which can be ascribed to the moderately dissociating power of the ACN solvent. The formation of such associations between the large $[Fe(tpen)]^{2+}$ complex and the Cl^- anions for this 0.136 M $[Fe(tpen)]Cl_2$ solution probably explains why the present solvation number of Cl^- of 6 is significantly smaller than the one of 9.5 determined by Fischer *et al.* for the anion in ACN at infinite dilution from Monte Carlo simulations.[88]

3.2 Dipole moments

The dipole distribution functions (DDFs) determined for $[Fe(tpen)]^{2+}$ in the two spin states are plotted in Fig. 13. The DDF calculated for LS $[Fe(tpen)]^{2+}$ is quite broad, the magnitude of the instantaneous dipole moment varying between 1 D and 7 D. The DDF is broader and shifted towards smaller values for HS $[Fe(tpen)]^{2+}$, the instantaneous dipole moment ranging from 0 D to 7 D. The dipole moments deduced from these DDFs for the solvated complex in the LS and in the HS state are 4.26 ± 0.99 D and 3.61 ± 1.07 D, respectively.

The DDFs of the solvent molecules in and beyond the first solvation shell of $[Fe(tpen)]^{2+}$ have also been determined. They are plotted in Fig. 13. The DDFs obtained for the ACN molecules in the bulk do not depend on the spin state of $[Fe(tpen)]^{2+}$. They lead to a molecular dipole moment of 4.90 ± 0.26 D, which is in good agreement with the experimental value of 4.5 ± 0.1 D determined for liquid ACN by Ohba and Ikawa.[89] The DDFs

obtained for the ACN molecule in the first solvation shell of $[Fe(tpen)]^{2+}$ are slightly shifted towards larger values, the shift being larger in the LS state than in the HS state. This reflects the spin-state dependence of the polarization of the solvation shell, which translates into dipole moments of 5.02 ± 0.27 D and 4.98 ± 0.27 D for the ACN molecules in the first solvation shell of $[Fe(tpen)]^{2+}$ in the LS and HS states, respectively.

3.3 Vibrational properties

Fig. 14 shows the calculated LS and HS 310 K IR spectra of $[Fe(tpen)]^{2+}$ in ACN. They have similar shapes and the intensity of the IR absorption bands tends to be stronger in the HS state than in the LS state, as illustrated by the plot of the HS-LS difference spectrum which could be use as a reference in transient IR absorption spectroscopy studies. The absorption peak present in the LS and HS spectra at 2290 cm^{-1} is reminiscent of the intense ν_2 C≡N stretching absorption band of ACN located at this same wavenumber (Fig. S10†). Its contribution to the spectra cancels out in the HS-LS difference spectrum.

4 Conclusion and outlook

The present AIMD study allowed us to achieve a detailed characterization of the $[Fe(tpen)]^{2+}$ SCO complex in ACN. The determination of its solution structure in the LS and in the HS state gave results in excellent agreement with those recently obtained by high-resolution TXAS.[37] Insights could be gained into the solvation structure of the complex and its spin-state dependence. Thus, the first solvation shell of $[Fe(tpen)]^{2+}$ consists of ACN molecules located in the grooves defined by the chelating coordination motif of the tpen ligand. Furthermore, upon the LS to HS change of states, the solvation number of $[Fe(tpen)]^{2+}$ increases from ≈9.2 to ≈11.9 and an inner solvation shell is formed. The LS and HS IR spectra of $[Fe(tpen)]^{2+}$ have been calculated and the AIMD approach used for the calculation allowed to directly take into account thermal, anharmonic and vibrational effects.[90–94] The two spectra show similar shapes, with an increase of the intensity of the absorption bands on going from the LS to the HS state. This same feature was observed for the LS and HS spectra similarly calculated for $[Fe(bpy)_3]^{2+}$ and $[Fe(tpy)_2]^{2+}$ in water.[43,46]

The three solvated complexes have also in common that their atomic disorder depends on their spin state and on the exposure of the observed atoms to the solvent. More generally, their thermal fluctuation turns out to be stronger the weaker the metal–ligand bonds, whose strength and directionality, in conjunction with the rigidity of the coordinating ligands, seem to dictate the directionality of the atomic displacements. A strong interpenetration between the coordination sphere and the solvation shell is observed for the three complexes as well. For $[Fe(tpen)]^{2+}$ in ACN, the entanglement is such that an inner solvation shell is formed on passing from the LS to the HS state. About one ACN molecule is associated with this inner solvation shell and it is located in the internal cavity which results from the arrangement of the 4 pyridine rings. This cavity becomes accessible in the HS state only thanks the structural changes undergone by $[Fe(tpen)]^{2+}$ upon the LS → HS change of state. The inner shell corresponds to the presence of an ACN molecule in the close vicinity of the Fe(II) ion with its N_{ACN} head directed towards the Fe(II) ion, a situation which thereafter can lead to the formation of a bond between the ACN molecule and the Fe(II) ion, that is, to its heptacoordination. The racemization of $[Fe(tpen)]^{2+}$ and of other chiral SCO Fe(II) complexes is proposed to be coupled with the SCO equilibrium.[48–51] The identification of the inner solvation shell of HS $[Fe(tpen)]^{2+}$ suggests that the enantiomerization of the complex in the HS state could be significantly assisted by the solvent.

In their electrochemical study of the activation of O_2 by $[Fe(tpen)]^{2+}$ under reductive conditions, Ségaud *et al.*[54] have found that the reaction starts with the formation of a complex between $[Fe(tpen)]^{2+}$ and O_2. On the basis of the present results, it is likely that this $[Fe(tpen)]^{2+}$–O_2 complex results from the occupancy of the internal cavity of HS $[Fe(tpen)]^{2+}$ by the dioxygen molecule. Interestingly also, Roncaroli and Meier investigated the kinetics of the reaction NO with $[Fe(tpen)]^{2+}$ and also with a SCO and a LS derivative of $[Fe(tpen)]^{2+}$.[53] Quantitative reactions leading to the formation of a complex with NO were observed for the SCO complexes only, and for $[Fe(tpen)]^{2+}$, the formation of the HS nitrosylated $[Fe(tpen)NO]^{2+}$ was evidenced by EPR spectroscopy. The reactions were found to exhibit a second-order kinetics and the authors proposed a mechanism wherein the reaction proceeds through the displacement of a water solvent molecule in the HS heptacoordinated $[Fe(tpen)OH_2]^{2+}$ species.[53] The finding of the inner solvation shell of HS $[Fe(tpen)]^{2+}$ advocates for this mechanism. From there, it appears that the extension of the present AIMD study to the one in the LS and HS states of the enantiomerization of $[Fe(tpen)]^{2+}$ in ACN and of its reaction with dioxygen, nitric oxide or superoxide[52] would provide valuable insights into the spin-state dependence of the reactivity of $[Fe(tpen)]^{2+}$ and its derivatives in solution.

Conflicts of interest

There are no conflicts to declare.

Acknowledgements

This work was supported by grants from the Swiss National Supercomputing Centre (CSCS) under projects ID s501 and s894, and from the Center for Advanced Modeling Science (CADMOS) under Project ID CTESIM. LMLD thanks Sophie Canton and Hans Hagemann for fruitful discussions.

References

1 *Spin Crossover in Transition Metal Compounds I-III*, ed. P. Gütlich and H. A. Goodwin, Springer-Verlag, Heidelberg, 2004, vol. 233–235.
2 J. J. McGarvey and I. Lawthers, *J. Chem. Soc., Chem. Commun.*, 1982, 906–907.
3 S. Decurtins, P. Gütlich, C. P. Köhler, H. Spiering and A. Hauser, *Chem. Phys. Lett.*, 1984, **105**, 1–4.

4 A. Hauser, *Top. Curr. Chem.*, 2004, **234**, 155–198.
5 A. Hauser and C. Reber, *Struct. Bonding*, 2016, **172**, 291–312.
6 C. Daniel, *Coord. Chem. Rev.*, 2015, **282–283**, 19–32.
7 T. J. Penfold, E. Gindensperger, C. Daniel and C. M. Marian, *Chem. Rev.*, 2018, **118**, 6975–7025.
8 C. Brady, P. L. Callaghan, Z. Ciunik, C. G. Coates, A. Døssing, A. Hazell, J. J. McGarvey, S. Schenker, H. Toftlund, A. X. Trautwein, H. Winkler and J. A. Wolny, *Inorg. Chem.*, 2004, **43**, 4289–4299.
9 M. M. N. Wolf, C. S. R. Groß, J. A. Wolny, V. Schünemann, A. Døssing, H. Paulsen, J. J. McGarvey and R. Diller, *Phys. Chem. Chem. Phys.*, 2008, **10**, 4264–4273.
10 A. L. Smeigh, M. Creelman, R. A. Mathies and J. K. McCusker, *J. Am. Chem. Soc.*, 2008, **130**, 14105–14107.
11 J. E. Monat and J. K. McCusker, *J. Am. Chem. Soc.*, 2000, **122**, 4092–4097.
12 W. Gawelda, A. Cannizzo, V.-T. Pham, F. van Mourik, C. Bressler and M. Chergui, *J. Am. Chem. Soc.*, 2007, **129**, 8199–8206.
13 A. Lapini, P. Foggi, L. Bussotti, R. Righini and A. Dei, *Inorg. Chim. Acta*, 2008, **361**, 3937–3943.
14 C. Consani, M. Prémont-Schwarz, A. ElNahhas, C. Bressler, F. van Mourik, A. Cannizzo and M. Chergui, *Angew. Chem., Int. Ed.*, 2009, **48**, 7184–7187.
15 G. Auböck and M. Chergui, *Nat. Chem.*, 2015, **7**, 629–633.
16 A. Moguilevski, M. Wilke, G. Grell, S. I. Bokarev, S. G. Aziz, N. Engel, A. A. Raheem, O. Kühn, I. Y. Kiyan and E. F. Aziz, *ChemPhysChem*, 2016, **18**, 465–469.
17 A. Ould Hamouda, F. Dutin, J. Degert, M. Tondusson, A. Naim, P. Rosa and E. Freysz, *J. Phys. Chem. Lett.*, 2019, **10**, 5975–5982.
18 M. Khalil, M. A. Marcus, A. L. Smeigh, J. K. McCusker, H. H. W. Chong and R. W. Schoenlein, *J. Phys. Chem. A*, 2006, **110**, 38–44.
19 W. Gawelda, V.-T. Pham, M. Benfatto, Y. Zaushitsyn, M. Kaiser, D. Grolimund, S. L. Johnson, R. Abela, A. Hauser, C. Bressler and M. Chergui, *Phys. Rev. Lett.*, 2007, **98**, 057401.
20 W. Gawelda, V.-T. Pham, R. M. van der Veen, D. Grolimund, R. Abela, M. Chergui and C. Bressler, *J. Chem. Phys.*, 2009, **130**, 124520.
21 C. Bressler, C. Milne, V.-T. Pham, A. ElNahhas, R. M. van der Veen, W. Gawelda, S. Johnson, P. Beaud, D. Grolimund, M. Kaiser, C. N. Borca, G. Ingold, R. Abela and M. Chergui, *Science*, 2009, **323**, 489–492.
22 G. Vankó, P. Glatzel, V.-T. Pham, R. Abela, D. Grolimund, C. N. Borca, S. L. Johnson, C. J. Milne and C. Bressler, *Angew. Chem., Int. Ed.*, 2010, **49**, 5910–5912.
23 S. Nozawa, T. Sato, M. Chollet, K. Ichiyanagi, A. Tomita, H. Fujii, S. ichi Adachi and S. ya Koshihara, *J. Am. Chem. Soc.*, 2010, **132**, 61–63.
24 N. Huse, T. K. Kim, L. Jamula, J. K. McCusker, F. M. F. de Groot and R. W. Schoenlein, *J. Am. Chem. Soc.*, 2010, **132**, 6809–6816.
25 N. Huse, H. Cho, K. Hong, L. Jamula, F. M. F. de Groot, T. K. Kim, J. K. McCusker and R. W. Schoenlein, *J. Phys. Chem. Lett.*, 2011, **2**, 880–884.
26 K. Haldrup, G. Vankó, W. Gawelda, A. Galler, G. Doumy, A. M. March, E. P. Kanter, A. Bordage, A. Dohn, T. B. van Driel, K. S. Kjær, H. T. Lemke, S. E. Canton, J. Uhlig, V. Sundström, L. Young, S. H. Southworth, M. M. Nielsen and C. Bressler, *J. Phys. Chem. A*, 2012, **116**, 9878–9887.
27 H. T. Lemke, C. Bressler, L. X. Chen, D. M. Fritz, K. J. Gaffney, A. Galler, W. Gawelda, K. Haldrup, R. W. Hartsock, H. Ihee, J. Kim, K. H. Kim, J. H. Lee, M. M. Nielsen, A. B. Stickrath, W. Zhang, D. Zhu and M. Cammarata, *J. Phys. Chem. A*, 2013, **117**, 735–740.
28 S. E. Canton, X. Zhang, L. M. Lawson Daku, A. L. Smeigh, J. Zhang, Y. Liu, C.-J. Wallentin, K. Attenkofer, G. Jennings, C. A. Kurtz, D. Gosztola, K. Wärnmark, A. Hauser and V. Sundström, *J. Phys. Chem. C*, 2014, **118**, 4536–4545.
29 W. Zhang, R. Alonso-Mori, U. Bergmann, C. Bressler, M. Chollet, A. Galler, W. Gawelda, R. G. Hadt, R. W. Hartsock, T. Kroll, K. S. Kjaer, K. Kubicek, H. T. Lemke, H. W. Liang, D. A. Meyer, M. M. Nielsen, C. Purser, J. S. Robinson, E. I. Solomon, Z. Sun, D. Sokaras, T. B. van Driel, G. Vanko, T.-C. Weng, D. Zhu and K. J. Gaffney, *Nature*, 2014, **509**, 345–348.
30 X. Zhang, M. L. Lawson Daku, J. Zhang, K. Suarez-Alcantara, G. Jennings, C. A. Kurtz and S. E. Canton, *J. Phys. Chem. C*, 2015, **119**, 3312–3321.
31 S. E. Canton, X. Zhang, M. L. Lawson Daku, Y. Liu, J. Zhang and S. Alvarez, *J. Phys. Chem. C*, 2015, **119**, 3322–3330.
32 G. Vankó, A. Bordage, M. Pápai, K. Haldrup, P. Glatzel, A. M. March, G. Doumy, A. Britz, A. Galler, T. Assefa, D. Cabaret, A. Juhin, T. B. van Driel, K. S. Kjær, A. Dohn, K. B. Møller, H. T. Lemke, E. Gallo, M. Rovezzi, Z. Németh, E. Rozsályi, T. Rozgonyi, J. Uhlig, V. Sundström, M. M. Nielsen, L. Young, S. H. Southworth, C. Bressler and W. Gawelda, *J. Phys. Chem. C*, 2015, **119**, 5888–5902.
33 K. Haldrup, W. Gawelda, R. Abela, R. Alonso-Mori, U. Bergmann, A. Bordage, M. Cammarata, S. E. Canton, A. O. Dohn, T. B. van Driel, D. M. Fritz, A. Galler, P. Glatzel, T. Harlang, K. S. Kjær, H. T. Lemke, K. B. Møller, Z. Németh, M. Pápai, N. Sas, J. Uhlig, D. Zhu, G. Vankó, V. Sundström, M. M. Nielsen and C. Bressler, *J. Phys. Chem. B*, 2016, **120**, 1158–1168.
34 B. E. Van Kuiken, H. Cho, K. Hong, M. Khalil, R. W. Schoenlein, T. K. Kim and N. Huse, *J. Phys. Chem. Lett.*, 2016, **7**, 465–470.
35 H. T. Lemke, K. S. Kjær, R. Hartsock, T. B. van Driel, M. Chollet, J. M. Glownia, S. Song, D. Zhu, E. Pace, S. F. Matar, M. M. Nielsen, M. Benfatto, K. J. Gaffney, E. Collet and M. Cammarata, *Nat. Commun.*, 2017, **8**, 15342.
36 C. Liu, J. Zhang, L. M. Lawson Daku, D. Gosztola, S. E. Canton and X. Zhang, *J. Am. Chem. Soc.*, 2017, **139**, 17518–17524.
37 J. Zhang, X. Zhang, K. Suarez-Alcantara, G. Jennings, C. A. Kurtz, L. M. Lawson Daku and S. E. Canton, *ACS Omega*, 2019, **4**, 6375–6381.
38 D. Khakhulin, L. M. Lawson Daku, D. Leshchev, G. E. Newby, M. Jarenmark, C. Bressler, M. Wulff and S. E. Canton, *Phys. Chem. Chem. Phys.*, 2019, **21**, 9277–9284.

39 K. S. Kjær, T. B. Van Driel, T. C. B. Harlang, K. Kunnus, E. Biasin, K. Ledbetter, R. W. Hartsock, M. E. Reinhard, S. Koroidov, L. Li, M. G. Laursen, F. B. Hansen, P. Vester, M. Christensen, K. Haldrup, M. M. Nielsen, A. O. Dohn, M. I. Pápai, K. B. Møller, P. Chabera, Y. Liu, H. Tatsuno, C. Timm, M. Jarenmark, J. Uhlig, V. Sundström, K. Wärnmark, P. Persson, Z. Németh, D. S. Szemes, É. Bajnóczi, G. Vankó, R. Alonso-Mori, J. M. Glownia, S. Nelson, M. Sikorski, D. Sokaras, S. E. Canton, H. T. Lemke and K. J. Gaffney, *Chem. Sci.*, 2019, **10**, 5749–5760.

40 A. Britz, W. Gawelda, T. A. Assefa, L. L. Jamula, J. T. Yarranton, A. Galler, D. Khakhulin, M. Diez, M. Harder, G. Doumy, A. M. March, É. Bajnóczi, Z. Németh, M. Pápai, E. Rozsályi, D. Sárosiné Szemes, H. Cho, S. Mukherjee, C. Liu, T. K. Kim, R. W. Schoenlein, S. H. Southworth, L. Young, E. Jakubikova, N. Huse, G. Vankó, C. Bressler and J. K. McCusker, *Inorg. Chem.*, 2019, **58**, 9341–9350.

41 M. A. Naumova, A. Kalinko, J. W. L. Wong, S. Alvarez Gutierrez, J. Meng, M. Liang, M. Abdellah, H. Geng, W. Lin, K. Kubicek, M. Biednov, F. Lima, A. Galler, P. Zalden, S. Checchia, P.-A. Mante, J. Zimara, D. Schwarzer, S. Demeshko, V. Murzin, D. Gosztola, M. Jarenmark, J. Zhang, M. Bauer, M. L. Lawson Daku, D. Khakhulin, W. Gawelda, C. Bressler, F. Meyer, K. Zheng and S. E. Canton, *J. Chem. Phys.*, 2020, **152**, 214301.

42 L. M. Lawson Daku and A. Hauser, *J. Phys. Chem. Lett.*, 2010, **1**, 1830–1835.

43 L. M. Lawson Daku, *Phys. Chem. Chem. Phys.*, 2018, **20**, 6236–6253.

44 A. K. Das, R. V. Solomon, F. Hofmann and M. Meuwly, *J. Phys. Chem. B*, 2016, **120**, 206–216.

45 S. Iuchi, *J. Chem. Phys.*, 2012, **136**, 064519.

46 L. M. Lawson Daku, *Phys. Chem. Chem. Phys.*, 2019, **21**, 650–661.

47 H. R. Chang, J. K. McCusker, H. Toftlund, S. R. Wilson, A. X. Trautwein, H. Winkler and D. N. Hendrickson, *J. Am. Chem. Soc.*, 1990, **112**, 6814–6827.

48 K. F. Purcell, *J. Am. Chem. Soc.*, 1979, **101**, 5147–5152.

49 L. G. Vanquickenborne and K. Pierloot, *Inorg. Chem.*, 1981, **20**, 3673–3677.

50 J. J. McGarvey, I. Lawthers, K. Heremans and H. Toftlund, *Inorg. Chem.*, 1990, **29**, 252–256.

51 J. K. McCusker, A. L. Rheingold and D. N. Hendrickson, *Inorg. Chem.*, 1996, **35**, 2100–2112.

52 M. Tamura, Y. Urano, K. Kikuchi, T. Higuchi, M. Hirobe and T. Nagano, *Chem. Pharm. Bull.*, 2000, **48**, 1514–1518.

53 F. Roncaroli and R. Meier, *J. Coord. Chem.*, 2015, **68**, 2990–3002.

54 N. Ségaud, E. Anxolabéhère-Mallart, K. Sénéchal-David, L. Acosta-Rueda, M. Robert and F. Banse, *Chem. Sci.*, 2015, **6**, 639–647.

55 M. J. Abraham, T. Murtola, R. Schulz, S. Páll, J. C. Smith, B. Hess and E. Lindahl, *SoftwareX*, 2015, **1–2**, 19–25.

56 B. Hess, C. Kutzner, D. van der Spoel and E. Lindahl, *J. Chem. Theory Comput.*, 2008, **4**, 435–447.

57 W. L. Jorgensen, D. S. Maxwell and J. Tirado-Rives, *J. Am. Chem. Soc.*, 1996, **118**, 11225–11236.

58 W. L. Jorgensen and N. A. McDonald, *J. Mol. Struct.: THEOCHEM*, 1998, **424**, 145–155.

59 W. L. Jorgensen and N. A. McDonald, *J. Phys. Chem. B*, 1998, **102**, 8049–8059.

60 R. C. Rizzo and W. L. Jorgensen, *J. Am. Chem. Soc.*, 1999, **121**, 4827–4836.

61 C. Caleman, P. J. van Maaren, M. Hong, J. S. Hub, L. T. Costa and D. van der Spoel, *J. Chem. Theory Comput.*, 2012, **8**, 61–74.

62 D. van der Spoel, P. J. van Maaren and C. Caleman, *Bioinformatics*, 2012, **28**, 752–753.

63 A. Ribeiro, B. Horta and R. de Alencastro, *J. Braz. Chem. Soc.*, 2008, **19**, 1433–1435.

64 A. D. Becke, *Phys. Rev. A: At., Mol., Opt. Phys.*, 1988, **38**, 3098–3100.

65 C. Lee, W. Yang and R. G. Parr, *Phys. Rev. B: Condens. Matter Mater. Phys.*, 1988, **37**, 785–789.

66 S. Grimme, J. Antony, S. Ehrlich and H. Krieg, *J. Chem. Phys.*, 2010, **132**, 154104.

67 G. Lippert, J. Hutter and M. Parrinello, *Mol. Phys.*, 1997, **92**, 477–487.

68 J. VandeVondele, M. Krack, M. Fawzi, M. Parrinello, T. Chassaing and J. Hutter, *Comput. Phys. Commun.*, 2005, **167**, 103–128.

69 S. Goedecker, M. Teter and J. Hutter, *Phys. Rev. B: Condens. Matter Mater. Phys.*, 1996, **54**, 1703–1710.

70 C. Hartwigsen, S. Goedecker and J. Hutter, *Phys. Rev. B: Condens. Matter Mater. Phys.*, 1998, **58**, 3641–3662.

71 M. Krack, *Theor. Chem. Acc.*, 2005, **114**, 145–152.

72 J. VandeVondele and J. Hutter, *J. Chem. Phys.*, 2007, **127**, 114105.

73 G. J. Martyna, M. L. Klein and M. Tuckerman, *J. Chem. Phys.*, 1992, **97**, 2635–2643.

74 N. Marzari, A. A. Mostofi, J. R. Yates, I. Souza, I. Souza and D. Vanderbilt, *Rev. Mod. Phys.*, 2012, **85**, 1419–1475.

75 M. Brehm and B. Kirchner, *J. Chem. Inf. Model.*, 2011, **51**, 2007–2023.

76 M. Brehm, M. Thomas, S. Gehrke and B. Kirchner, *J. Chem. Phys.*, 2020, **152**, 164105.

77 M. Thomas, M. Brehm and B. Kirchner, *Phys. Chem. Chem. Phys.*, 2015, **17**, 3207–3213.

78 K. A. F. Röhrig and T. D. Kühne, *Phys. Rev. E: Stat., Nonlinear, Soft Matter Phys.*, 2013, **87**, 045301.

79 W. Humphrey, A. Dalke and K. Schulten, *J. Mol. Graphics*, 1996, **14**, 33–38.

80 J. Stone, MSc thesis, Computer Science Department, University of Missouri-Rolla, 1998.

81 *Jmol: an open-source Java viewer for chemical structures in 3D*, http://www.jmol.org, accessed November 2, 2017.

82 B. McMahon and R. M. Hanson, *J. Appl. Crystallogr.*, 2008, **41**, 811–814.

83 R. M. Hanson, J. Prilusky, Z. Renjian, T. Nakane and J. L. Sussman, *Isr. J. Chem.*, 2013, **53**, 207–216.

84 J. D. Hunter, *Comput. Sci. Eng.*, 2007, **9**, 90–95.

85 A. Hauser, C. Enachescu, M. Lawson Daku, A. Vargas and N. Amstutz, *Coord. Chem. Rev.*, 2006, **250**, 1642–1652.
86 S. Pothoczki and L. Pusztai, *J. Mol. Liq.*, 2017, **225**, 160–166.
87 J. Hernández-Cobos, J. M. Martínez, R. R. Pappalardo, I. Ortega-Blake and E. Sánchez Marcos, *J. Mol. Liq.*, 2020, **318**, 113975.
88 R. Fischer, J. Richardi, P. H. Fries and H. Krienke, *J. Chem. Phys.*, 2002, **117**, 8467–8478.
89 T. Ohba and S. Ikawa, *Mol. Phys.*, 1991, **73**, 985–997.
90 A. J. R. da Silva, J. W. Pang, E. A. Carter and D. Neuhauser, *J. Phys. Chem. A*, 1998, **102**, 881–885.
91 R. Ramírez, T. López-Ciudad, P. Kumar P and D. Marx, *J. Chem. Phys.*, 2004, **121**, 3973–3983.
92 M.-P. Gaigeot, *J. Phys. Chem. A*, 2008, **112**, 13507–13517.
93 M. Kaledin, J. M. Moffitt, C. R. Clark and F. Rizvi, *J. Chem. Theory Comput.*, 2009, **5**, 1328–1336.
94 S. D. Ivanov, A. Witt and D. Marx, *Phys. Chem. Chem. Phys.*, 2013, **15**, 10270–10299.